SOLAR CELLS

Redirecting wet-interfacial redox pathways for efficient inverted perovskite solar cells

Zheng Liang[1,2]†, Boyuan Liu[3,4]†, Yuelong Li[5,6]†, Yalan Zhang[2]†, Yi Yang[7]†, Shengbin Cheng[1], Linchuan Ma[5], Bao Tu[8], Hua-Chao Liu[9], Huifen Xu[3], Yuqi Bao[1], Minghui Fan[3], Peide Zhu[10], Xianfu Zhang[11], Congqi Li[12], Hui Zhang[3,4], Xinyuan Zhang[4], Yuheng Li[1], Guodong Chen[8], Cheng Liu[11]*, Chen Zhu[8]*, Chuying Ouyang[8], Nam-Gyu Park[2,13]*, Yong Zhang[1]*

Carbazole-based phosphonic acid self-assembled monolayers (SAMs) are essential for high-efficiency p-i-n perovskite solar cells. However, during processing, these SAMs inevitably contact perovskite inks, where their acidity triggers a dimethyl sulfoxide (DMSO)-mediated iodide redox reaction that imprints device performance, representing a universal bottleneck for inverted devices. We resolve this SAM-triggered redox mechanism and introduce chemistry-matched hydrazide additives to mitigate the degradation. These additives abrogate DMSO activation and redirect unwanted by-products toward benign hydrazide–formamidinium adducts. Consequently, we achieved power conversion efficiencies (PCEs) of 27.7% (certified 27.4%) in small-area (0.06 cm^2) cells and 20.1% in 2.0 m^2 modules, along with T95 lifetimes of ~2000 hours of maximum power point tracking (MPPT) at 85°C and ~1500 hours MPPT at 85°C and 85% relative humidity.

Carbazole-based phosphonic acid self-assembled molecules (SAMs) used as hole-selective contacts in p-i-n perovskite solar cells (PSCs) have registered steady performance gains (*1*–*12*). In this family of SAMs, a carbazole-derived motif enables efficient hole transport, and interfacial hydrogen-bonding and coordination interactions bind the terminal phosphonic acid headgroup to transparent conductive substrates (*13*–*15*). These SAMs have enabled PSCs to reach certified power conversion efficiencies (PCEs) of 27.2% (*1*).

Despite these advances, SAMs anchoring in practice is often insufficiently strong or uniform to create a single, well-ordered monolayer. Instead, SAMs frequently assemble into multilayers containing a fraction of loosely stacked molecules, yielding an ultrathin interlayer on the nanoscale (*5*–*8*). Therefore, SAM contacts remain chemically dynamic interfaces. Their molecular nature renders them susceptible to desorption, aggregation, and interfacial reconstruction under operational stress, which can degrade charge extraction and long-term stability (*12*, *16*–*18*).

Recent studies further suggest that partial SAM desorption and the intrinsic acidity of phosphonic acid anchoring groups can disrupt the underlying perovskite lattice during aging. Accordingly, redesigning SAM structures to strengthen substrate binding has therefore proven effective in mitigating post-fabrication degradation and improving operational durability (*19*). However, current understanding is largely confined to degradation processes that occur after device completion. Whether the intrinsic acidity of phosphonic acid SAMs influences the wet-chemical environment prior to, and during, perovskite film formation remains relatively unexplored. This gap is critical, because solution-processed perovskite deposition—a key determinant of crystallization dynamics and ultimate device performance (*19*)—inherently involves prolonged contact between polar precursor inks and the SAM-modified substrate. If acidic species come into contact with or leach into the precursor ink, they can alter precursor speciation and influence crystallization before film solidification.

Here, we show that the impact of SAM acidity begins well before device aging. Upon contact with dimethyl sulfoxide (DMSO)-containing precursor solutions under typical processing conditions, SAM-derived acidity participates in solution reactions that trigger and accelerate DMSO-mediated iodide oxidation and form reactive iodine species and iodine–solvent adducts. These by-products emerge on timescales comparable to coating and annealing, become incorporated during crystallization, and preferentially perturb the buried interface (*20*). The resulting interfacial lattice distortion and iodine-related deep defects degrade film quality, suppress PCE, and compromise stability. Notably, these effects intensify under the extended wet-processing windows required for large-area manufacturing, where interfacial solution chemistry becomes increasingly consequential (*21*).

Guided by this mechanism, we developed a chemically compatible additive strategy that selectively scavenged SAM-derived protons and suppressed and redirected acid-driven redox pathways toward benign intermediates. The resulting interfacial species improved energetic continuity and facilitated vertical hole extraction. With this approach, we achieved a champion PCE of 27.7% (certified fast-scan efficiency of 27.6%, stabilized efficiency of 27.4%) for laboratory-scale devices and 20.1% for 2 m^2 modules. Device durability was substantially extended, with T95 lifetimes of ~2000 hours under ISOS L-2I condition at 85°C and ~1500 hours under ISOS L-3 condition at 85°C and 85% relative humidity (RH).

SAM-triggered chemistry in perovskite inks

To study the wet chemistry that generally emerges when carbazole–phosphonic acid SAMs engaging perovskite inks, we selected four widely used, structurally representative molecules (Fig. 1A): (2-(9H-carbazol-9-yl)ethyl)phosphonic acid (2PACz; Cz, **R1**), (2-(3,6-dimethoxy-9H-carbazol-9-yl)ethyl)phosphonic acid (MeO-2PACz; MeOCz, **R2**), (4-(7H-dibenzo[c,g]carbazol-7-yl)butyl)phosphonic acid (4PADCB; DBCz, **R3**), and (4-(3,6-dimethyl-9H-carbazol-9-yl)butyl)phosphonic acid (Me-4PACz; MeCz, **R4**). This set of SAMs spans structural variations in carbazole substitution and ensures the generality of our observations.

Visual inspections hinted at a rapid chemical transformation upon SAM addition. Even with very fresh solutions at room temperature in N_2, SAMs turned initially colorless formamidinium iodide (FAI)/DMSO solutions pale yellow and then darkened upon heating (Fig. 1B). Similar changes seen in methylammonium iodide (MAI)/DMSO and full precursor inks confirmed that this reactivity was general to SAM–perovskite ink interactions (figs. S1 to S3).

These color evolutions pointed to a very fast oxidation of iodide (I^-) to I_2/I_3^-, particularly in the DMSO solution containing acidic species

[1]Sustainable Energy and Environment Thrust, Guangzhou Municipal Key Laboratory of Materials Informatics, The Hong Kong University of Science and Technology (Guangzhou), Guangzhou, China. [2]School of Chemical Engineering and Center for Antibonding Regulated Crystals, Sungkyunkwan University, Suwon, Republic of Korea. [3]University of Science and Technology of China, Hefei, China. [4]Hefei Institutes of Physical Science, Chinese Academy of Sciences, Hefei, China. [5]Institute of Photoelectronic Thin Film Devices and Technology of Nankai University, Tianjin Key Laboratory of Efficient Utilization of Solar Energy, Engineering Research Center of Thin Film Optoelectronics Technology (MOE), State Key Laboratory of Photovoltaic Materials and Cells, College of Outstanding Engineers, and Academy for Advanced Interdisciplinary Studies, Nankai University, Tianjin, China. [6]Shenzhen Research Institute of Nankai University, Shenzhen, China. [7]Global Institute of Future Technology (GIFT), Shanghai Jiao Tong University, Shanghai, China. [8]Fujian Science and Technology Innovation Laboratory for Energy Devices of China (CATL 21C Lab), Ningde, China. [9]College of Materials Science and Engineering, Shenzhen University, Shenzhen, China. [10]Department of Materials Science and Engineering, Southern University of Science and Technology, Shenzhen, China. [11]Frontiers Science Center for Transformative Molecules, State Key Laboratory of Fluorine-Containing Functional Membrane Materials, Shanghai Jiao Tong University, Shanghai 200240, China. [13]College of Materials Science and Opto- Electronic Technology, University of Chinese Academy of Sciences, Beijing, China. [13]SKKU National Lab for Intelligent Energy Solution Technology (SIEST), Sungkyunkwan University, Suwon, Republic of Korea. ***Corresponding author. Email: c.liu@sjtu.edu.cn (C.L.); aronzhu@catl-21c.com (C.Z.); npark@skku.edu (N.-G.P.); yongzhang@hkust-gz.edu.cn (Y.Z.)**
†These authors contributed equally to this work.

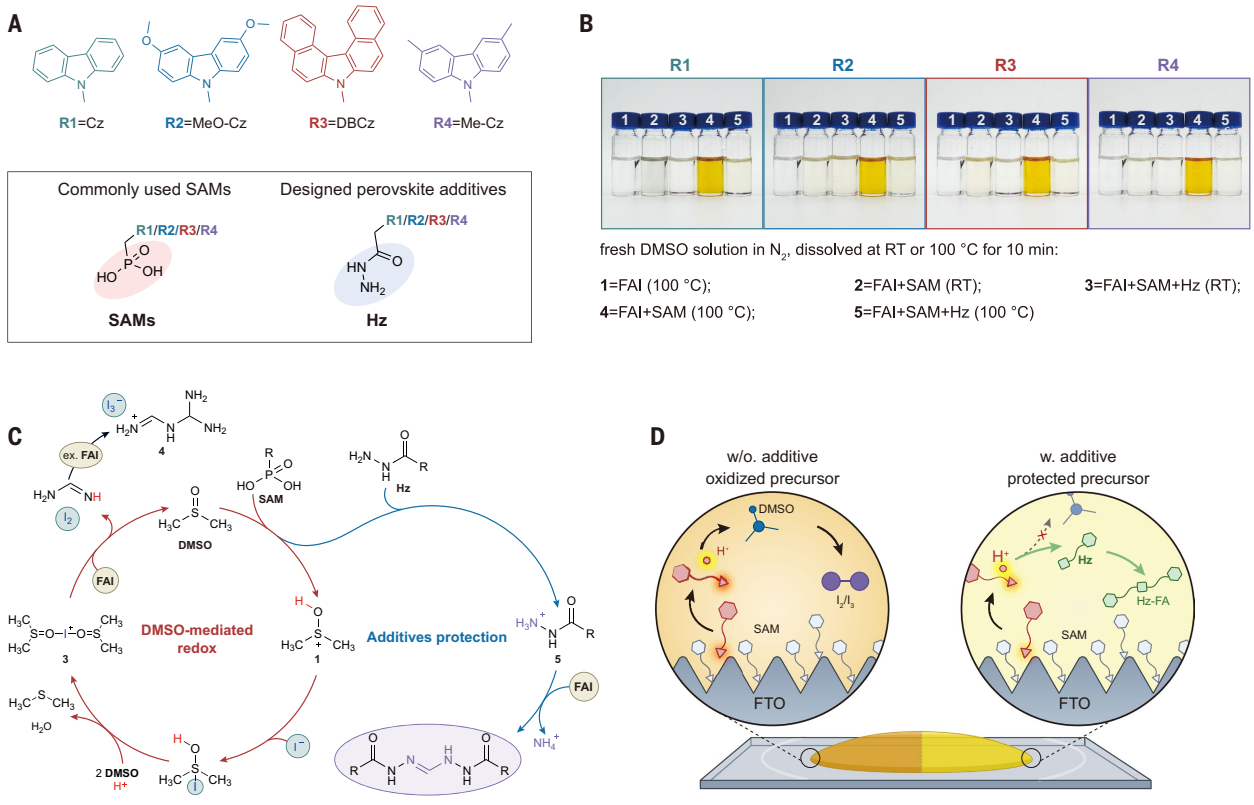

Fig. 1. Chemistry of perovskite precursors engaging SAMs. (**A**) Definitions of the R substituents and the general structures of commonly used SAMs and the designed perovskite additive molecules. (**B**) Photographs of the various FAI in DMSO solutions prepared at two dissolution temperatures. (**C**) Proposed reaction scheme for interactions between perovskite precursors, SAMs, and Hz molecules. (**D**) Schematic illustration of SAM and Hz involving side reactions in wet perovskite inks during film deposition.

(figs. S4 to S7) (*22*–*24*). DMSO is known to be only a weak oxidant (*22*, *23*), suggesting that the key driver of the enhanced reactivity is the presence of phosphonic acid species leached from SAMs into the ink. We therefore proposed that phosphonic acids introduced an alternative, proton-assisted pathway that accelerated an organic-iodide salts redox reaction, plausibly through protonating and activating DMSO and thereby enabling its role as a mediator for iodide oxidation (*25*).

Accordingly, we designed a set of four conjugated hydrazide-based additives (Hz) for perovskite precursors, to address this reaction at its origin (Fig. 1A). These additives share a general structure of R-propanehydrazide (R-Hz), where the R group mirrors the corresponding SAM chromophore to function with semiconducting properties and maintain compatibility with SAMs. Synthetic routes are provided in the methods and figs. S8 to S12. The terminal hydrazide functionality was chosen to buffer or capture the excess protons in the ink, thereby inhibiting proton-driven DMSO activation and the subsequent redox reaction. Consistently, adding the matched Hz from the outset markedly weakened the color evolutions across all DMSO-containing solutions (FAI, MAI, and full perovskite precursors), and in many cases kept the solutions essentially colorless (Fig. 1B and figs. S1 to S5). These results confirmed that hydrazide additives effectively intercepted the proton-driven reactivity triggered by leached SAMs.

Proton nuclear magnetic resonance (^{1}H NMR) measurements were performed to resolve the reaction underlying these observations. In pristine FAI, both the characteristic formamidinium cations (FA^+) C–H and N–H resonances appeared as singlets, consistent with a homogeneous chemical environment. After introducing any of the four SAMs, the FA^+ C–H resonance broadened and evolved from a singlet into multiplets, whereas the N–H signal split into two distinct peaks (figs. S13 and S14). These changes were consistent with a shifted protonation/exchange equilibrium and the emergence of chemically nonequivalent N–H environments in the presence of phosphonic acid species (*26*). Additionally, these spectral evolutions demonstrated stoichiometry-dependent trends (figs. S15 to S18), further supporting a direct chemical interaction between SAMs and FA^+. Complementary ^{13}C NMR revealed new carbon signals upon mixing FAI and SAMs in DMSO (figs. S19 to S22), suggesting that the FA^+ moiety underwent side reactions in the SAM-containing inks, likely forming reaction by-products.

By contrast, introducing Hz to the ternary FAI/SAM/Hz mixtures reverted the FA^+ C–H resonance to a clean singlet, and suppressed the doublets splitting of protonated N–H (indicated by an arrow in fig. S14) observed in FAI/SAM mixtures (fig. S14). Identical behaviors were observed for samples prepared in a DMF/DMSO cosolvent system (fig. S23). This result indicated that the Hz additives stabilized the chemical environment of FA^+ and inhibited the SAM-triggered side reactions. Both C–H and N–H resonances shifted noticeably downfield relative to the FAI/SAM samples (fig. S13), suggesting that Hz were not chemically inert but instead engaged in specific interactions with FA^+ species.

Two-dimensional (2D) ^{1}H–^{1}H correlation spectroscopy (COSY) measurements (fig. S24) confirmed that the Hz-containing sample exhibited distinctive cross-peaks linking the FA^+ C–H and N–H resonances. The appearance of these correlations compared to the FAI/SAM mixtures supported a direct coupling pathway enabled by Hz addition, suggesting reactive sites between FA^+ and Hz molecules, and further local or molecular structural alterations (*27*–*29*).

We used high-performance liquid chromatography–mass spectrometry (HPLC–MS) to directly track iodide oxidation in DMSO and DMF/DMSO solutions and resolve the molecular identities of the reaction (fig. S25). In pristine FAI/DMSO, only a weak I_3 signal at a mass-to-charge ratio m/z 381 was observed, accompanied by low-intensity FA_xI_y adducts that arise from association of FA species with iodide in mixed

valence states (fig. S26). Once SAMs were introduced, strong I_3 signals emerged, and the FA_xI_y series intensified substantially, including assignments consistent with FAI_2, FA_2I_3, and FA_3I_4 at *m/z* 299, 471, and 643, respectively. By contrast, in the corresponding ternary FAI/SAM/Hz samples, I_3 was no longer detectable and the FA_xI_y signals collapsed to near-background levels. These results directly showed that SAM-derived phosphonic acids promoted an iodide redox in DMSO, whereas Hz additives effectively shut down this deleterious pathway.

Two features stood out as fingerprints of the SAM-triggered chemistry (figs. S27 to S32). Peaks at *m/z* 282 and 89 appeared across all of the FAI/SAM samples, yet were absent once Hz was added. The *m/z* 282 species is consistent with a $(DMSO)_2$-I adduct (compound **3**) (*30*, *31*). The *m/z* 89 signal, by contrast, showed no multiplicative relationship expected for FA–FA coupling products, making FA^+ dimerization unlikely. Instead, this feature points to a by-product of FA^+. Guided by the accompanying NMR results, we tentatively assigned the *m/z* 89 product to molecular compound **4**, plausibly formed by nucleophilic addition of the C=N functionality at the terminal $-NH_2$ site of FA^+ (*32*, *33*). Notably, HPLC-MS analysis revealed that the intensities of compounds **3**, **4** and $\mathbf{I_2}/\mathbf{I_3}^-$—critical indicators in the redox pathway—exhibited a DMSO-stoichiometric dependence, implying the catalytic-like behavior of DMSO in mediating and propagating the redox cycle (figs. S33 to S35).

Critically, at similar retention times (≈10 min), new peaks appeared exclusively in the FAI/SAM/Hz samples, suggesting a common scaffold with R-dependent mass contributions. Each sample consistently produced two dominant new peaks: 281/517 (R1), 341/637 (R2), 381/717 (R3), and 309/573 (R4) (figs. S27 to S32). Together with the quantitative ^{1}H NMR integration analysis (fig. S36), we attributed these signals to products formed between Hz and FA^+, with molecular structure of R–Hz–CH=Hz–R (compound 6). These species were consistently detected in broader solvent systems (figs. S37 to S39).

Collectively, we propose a general chemistry scheme operative during film formation (Fig. 1C). In DMSO-containing perovskite inks, SAM-derived phosphonic acids introduced excess protons that activated DMSO to form DMSO–H^+ (**1**) through electrophilic reaction, which then generated a highly reactive iodine adduct (compound **2**). In presence of excess DMSO, this species converted into $(DMSO)_2$–I species (**3**), which accelerates iodide oxidation by releasing I_2 in a thermodynamically favorable pathway (fig. S42). The liberated I_2 is subsequently rapidly converted to I_3^- in the presence of excess I^-, while regenerating DMSO for propagating the next cycle.

Hz additives redirected the DMSO-mediated redox circle, the hydrazide group sequestered the SAM-derived protons, suppressing DMSO activation. Protonated Hz (**5**) could then react with FA^+ to form stable adducts. A plausible scheme involves two deamination steps (figs. S40 and S41) that ultimately couple two R-Hz fragments (*34*), yielding an R–Hz–CH=Hz–R structure (**6**). Density functional theory (DFT) free-energy calculations confirmed that Hz additives provided an energetically favorable route to suppress the SAM-triggered redox cycle (fig. S42).

During perovskite casting on SAM-coated substrates and throughout the subsequent annealing—a period during which the SAM molecules inevitably infiltrate the precursor ink (figs. S43, S44, and S53)—the contact between SAM and perovskite precursor enabled the above redox reaction that could proceed rapidly. It generated oxidized iodine species, solvent–halide adducts, and cation-derived by-products. These additional species can plausibly perturb nucleation and growth and their residues may persist in the solid film, ultimately degrading both structural integrity and optoelectronic quality.

By effectively trapping the undesirable protons, Hz additives redirected this chemistry and suppressed the accumulation of I_2/I_3^- and helped stabilize the organic-cation environment. At the same time, they promoted formation of semiconducting Hz–FA adducts that were conjugated with the SAM layer. In essence, the two reaction manifolds created distinct chemical landscapes in the wet ink. Early-stage differences had a lasting imprint on the microstructure and optoelectronic properties of the final perovskite film (Fig. 1D).

Impact of Hz additives

To probe the kinetics during film formation, we performed thermal in situ Raman spectroscopy on the corresponding solutions, accompanied by calculating the rate constant k through taking the time derivative of I_3 Raman intensity to quantitively compare the redox rate (fig. S45). Two diagnostic bands were tracked, 112 cm^{-1} and 673 cm^{-1}, which we assigned to I_3^- and vibration of DMSO (C-S bond), respectively (*35*, *36*). In pristine FAI/DMSO solution, the I_3^- band slightly increased within the first 20 min and then remained nearly constant during the subsequent 3 hours with a k value of 7.4 (Fig. 2A), indicating minimal intrinsic iodide oxidation.

By contrast, the I_3^- signal in FAI/SAM DMSO solutions substantially intensified at the early stage, and further increased continuously throughout the entire measurement period. An increased k value of 36.7 indicated rapid, sustained, SAM-promoted iodide oxidation. Simultaneously, the C–S band progressively decreased (Fig. 2B), consistent with ongoing DMSO consumption and transformation. When the Hz additive was introduced, both bands showed negligible evolution (Fig. 2C), with an I_3 k value of 2.3 that was below the intrinsic oxidization level, confirming effective suppression of the redox process. We note that these reactions occur on a timescale comparable to coating and annealing process of perovskite film formation. Measurements of perovskite precursor deposition on SAM-coated substrates, replicating the actual fabrication conditions, confirmed these redox processes. (fig. S46). As such, oxidized iodine species and iodine–DMSO adducts would be generated before film completion to influence the crystallizations (fig. S47) (*24*, *37*, *38*).

To assess the degree to which these reaction products distort the perovskite lattice, we calculated the destabilization energy (E_D) using DFT (figs. S48 and S49) (*39*). The parent SAM and Hz additive molecules exhibited small E_D values (0.10 and 0.07 eV, respectively), indicating minimal perturbation to the lattice. By contrast, oxidized I_2/I_3^- and the $(DMSO)_2$–I adduct strongly destabilized the perovskite lattice, with E_D values of 9.06 and 4.10 eV, respectively, implying their potential to induce defects and reduce crystallinity. The Hz-derived product **6** showed a slightly negative E_D (−0.04 eV), which suggested a stabilizing interaction with the perovskite framework.

We collected 2D grazing-incidence wide-angle x-ray scattering (GIWAXS) patterns from both the surface and the peeled-off bottom interface of perovskite layers deposited on the SAM substrates. Perovskite films deposited directly on bare FTO were measured as a control (figs. S50 and S51). Azimuthal integration of all surface patterns showed comparable preferred orientations at ~30° and ~60° across all samples, indicating similarly high crystallinity near the top surface (Fig. 2D). For the FTO/perovskite control, the bottom pattern closely resembled the surface. When perovskite was deposited on SAM substrates, however, the bottom region largely lost its orientational order, confirming interfacial lattice distortion and compromised crystallization. The bottom of the FTO/SAM/perovskite(Hz) film recovered the two-domain preferred orientation and showed higher scattering intensity (Fig. 2E), demonstrating that Hz additive suppresses interfacial distortion and promotes crystallization at the buried interface.

X-ray photoelectron spectroscopy (XPS) was performed under identical conditions from two interfaces (Fig. 2F and fig. S52). For the FTO/perovskite control, the C, N, Pb, and I core levels were essentially identical between the surface and bottom. By contrast, the FTO/SAM/perovskite sample showed differences between two interfaces. Relative to the control, the surface exhibited only a minor shift of the Pb and I peaks, whereas the buried interface displayed pronounced upshifts of +0.35 eV (I) and +0.24 eV (Pb). These higher binding energies indicated a more electron-deficient state environment. These results implied an increased population of undercoordinated Pb-related defects and the presence of iodine species in higher oxidation states (*40*).

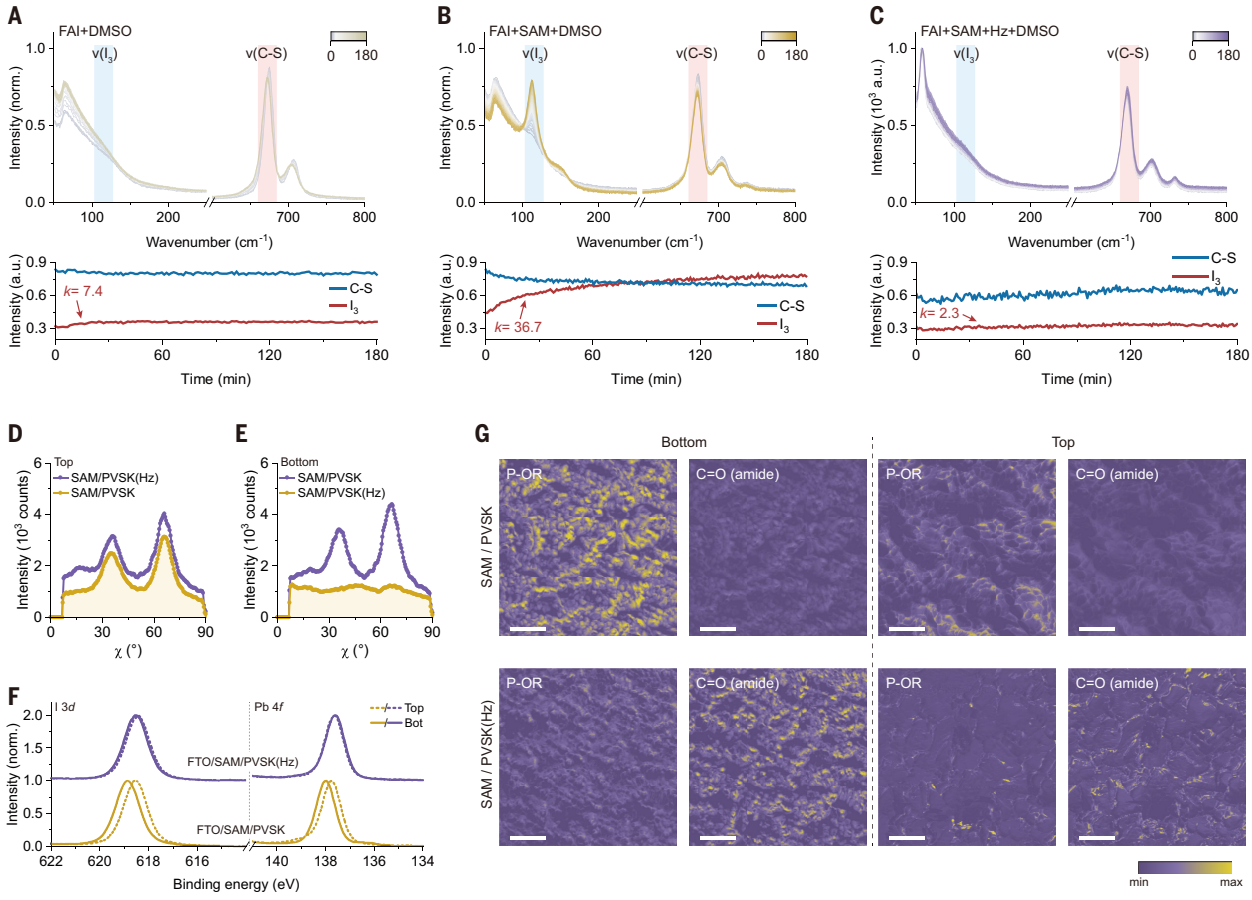

Fig. 2. Impact on perovskite films. (**A** to **C**) (Top) In situ Raman spectra of DMSO solutions heated at 100°C for (A) FAI, (B) FAI+SAM, and (C) FAI+SAM+Hz. Blue and red shaded regions highlight the I_3^- and C–S (DMSO) vibrational bands used for the intensity–time analysis, respectively. Lower panels show the corresponding intensity–time evolution with k obtained from fits to quantify reaction kinetics. (**D** and **E**) Integrated 1D intensity of the perovskite (100) reflection for azimuthal-angle analysis of films deposited on SAM substrates, measured from (D) the top surface and (E) the buried interface. (**F**) XPS spectra of the I *3d* and Pb *4f* core levels of perovskite films deposited on SAM substrates, acquired from the buried interface and the top surface as indicated by solid and dashed lines, respectively. (**G**) AFM–IR maps of perovskite films deposited on SAM substrates with and without Hz additive, collected from the top surface and the buried interface as indicated. Two characteristic vibrational responses assigned to P–OR and amide C=O are shown. Scale bar, 1 μm. Me-4PACz and MeCz-Hz are used as representative examples throughout this figure. a.u., arbitrary units.

Incorporating Hz additives largely eliminated this interfacial disparity. The surface and bottom spectra became closely aligned, and the Pb signal shifted toward lower binding energy, consistent with electron donation and coordination of Hz with the perovskite lattice (*41*).

To further resolve the local chemical environments underlying the interfacial discrepancies induced by SAM substrates, we performed atomic force microscope–infrared spectroscopy (AFM–IR) mapping (Fig. 2G). Two characteristic vibrational modes were tracked: 941 cm^{-1}, which we assigned to phosphate-related P–OR vibrations, and 1616 cm^{-1}, which we assigned to the amide C=O stretch of the Hz additives (fig. S53) (*42*). For the FTO/SAM/perovskite sample, the P–OR signal was detected at both interfaces. At the buried interface, large amount of P–OR signal was predominantly located at grain interiors. A reasonable explanation is that SAM (or deprotonated SAM anions) could adsorb on the perovskite lattice or form interfacial ion-pair structures ($FA^+\cdots SAM^-$), which may distort the lattice and impact charge transport (*43*). No amide C=O signal was observed in this sample. With Hz additives, the buried-interface P–OR signal was strongly suppressed, whereas the amide C=O signal became broadly distributed. These results are consistent with Hz preferentially scavenging the SAM-derived protons and reacting with FA^+ to form Hz–FA adducts (compound **6**), which then adsorbed more readily onto the perovskite lattice (fig. S54). At the surface, a small amount of P–OR was observed at grain boundaries, whereas Hz additives effectively helped in suppressing this diffusion by competitive adsorption. These spatially resolved distributions were further validated by time-of-flight secondary ion mass spectrometry (ToF-SIMS) measurements (fig. S55).

Charge transport

Charge-transfer pathways were studied by DFT differential charge-density analysis. Two structural models were constructed to capture a representative grain-boundary environment and the buried perovskite/SAM interface. At grain boundaries, an adsorbed SAM molecule mediated only limited hole transport, corresponding to a net transfer of 0.07 holes between adjacent perovskite grains (fig. S56). By contrast, the generated Hz–FA adduct (**6**) was bound through its oxygen atoms to form Pb–O bonds and its two headgroups R adhered to neighboring grains. Unlike adsorbed SAM molecules, the geometry of adsorbate **6** promoted hole withdrawal from both grains, and directed charge vertically toward the electrode. The total extraction of 0.6 holes per molecule (Fig. 3A) achieved a nearly ninefold enhancement relative to SAMs.

At the buried interface, SAM adsorbed on the perovskite lattice extracted 0.08 holes (fig. S57), whereas **6** increased the extracted charge to 0.36 holes (Fig. 3B). Notably, **6** adopted a relatively flat configuration at the perovskite/SAM heterojunction regardless of the specific oxygen binding site. In this configuration, one terminal R group coupled to the

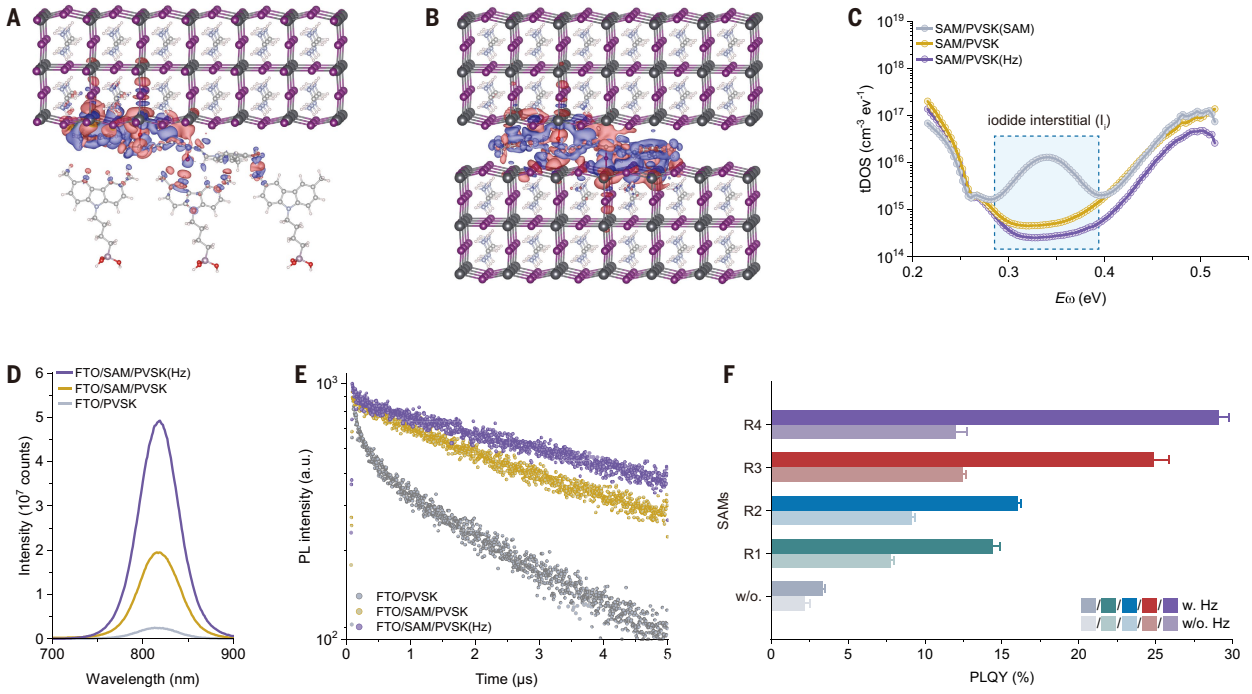

Fig. 3. Charge transport. (**A** and **B**) Charge-density difference maps of heterojunction anchoring compound 6 for (A) the SAM/perovskite interface and (B) a grain-boundary model. Blue indicates charge depletion and red indicates charge accumulation, and the same isosurface level is used for both panels. (**C**) Thermal admittance spectroscopy of devices with and without Hz additive, including a control device fabricated by directly adding the SAM molecule into the perovskite ink. (**D** and **E**) Photoluminescence (PL) of perovskite films with and without Hz additive deposited on different substrates, measured as (D) steady-state spectra and (E) time-resolved decays. (**F**) Photoluminescence quantum yield (PLQY) of perovskite films deposited on different substrates, with substrate types indicated on the *y* axis. Data are shown as mean ± standard error of the mean (SEM).

perovskite to extract holes, whereas the second R group—chemically matched to the R of SAM—facilitated onward transfer into the SAM layer. This two-sided coupling rationalizes our additive design strategy, in which the R group was intentionally conjugated to the parent SAM to maximize interfacial electronic continuity.

Heyd–Scuseria–Ernzerhof (HSE) calculations that included spin–orbit coupling (SOC) of projected density of states (pDOS) indicated that the Hz–FA adduct (**6**) compensated the interfacial energetic mismatch. At the SAM–perovskite heterojunction, the offset between perovskite valence-band maximum and the HOMO of adsorbed molecules decreased from 0.31 eV for the parent SAM to 0.12 eV for adduct **6**. At the grain boundaries, the corresponding offsets dropped from 0.58 eV (SAM) to 0.05 eV (**6**). The reduced energetic separation supported more efficient hole extraction enabled by the Hz–FA adducts (**6**) (*44*).

The calculated frontier energy levels of the key species explained the improved charge transfer (fig. S58). Both the Hz molecules and the Hz–FA adducts **6** exhibit HOMO levels that lie between those of the SAM and the perovskite valence-band maximum (fig. S59). This energy alignment can bridge the energetic offset at heterojunction structure, lowering the barrier for hole extraction and supporting more efficient charge transport.

Besides charge transfer, defects induced nonradiative recombination. We performed thermal admittance spectroscopy to directly probe trap states (Fig. 3C). Relative to the additive-free device, the Hz-containing sample showed little change in the shallower trap density of states (tDOS) near 0.25 to 0.30 eV, but it did show a reduction in the deeper region (0.30 to 0.50 eV), indicating Hz additives effectively passivated deep traps. This deep energy window of ~0.30 to 0.40 eV is strongly associated with iodine-interstitial–related defects arising from oxidized iodine species of SAM-triggered redox (*24*, *45*, *46*), which is confirmed by the sample that intentionally intensified redox reaction (gray line). The spatial distribution of these defects was well correlated with our drive-level capacitance profiling and ToF-SIMS profiles (fig. S60).

Steady-state photoluminescence (PL) measurements corroborated these trap-passivation effects. For all four SAMs, PL intensities increased when perovskite was deposited on SAM-modified substrates relative to bare FTO, and emission intensity was further enhanced by roughly a factor of 2 upon introducing the corresponding Hz additive (Fig. 3D and fig. S61). Although SAMs function as hole-transporting layers (HTLs), the strengthened PL in the half-stack configuration (FTO/SAM/perovskite) can be explained by reduced nonradiative recombination dominating interfacial quenching (*5*).

PL mapping revealed a markedly more uniform emission landscape for films processed with Hz additives. At the buried interface, the PL intensity increased substantially upon Hz incorporation, consistent with reduced interfacial nonradiative recombination (fig. S62). These observations were consistent with the suppressed redox cycle that redirected the chemistry through Hz-assisted pathways that extended the processing window for perovskite inks on SAM-coated substrates. The ink can remain in contact with the interface for longer without accumulating detrimental by-products, which helps preserve film quality and improve coating uniformity over large areas.

Transient PL (tr-PL) measurements (fig. S63 and table S1) showed that all SAM-based half stacks exhibited longer carrier lifetimes than the FTO/perovskite sample, and lifetimes increased further with Hz additives. For Me-4PACz, the lifetime rose from 2.20 μs (FTO/perovskite) to 3.01 μs (FTO/Me-4PACz/perovskite), and reached 5.75 μs after adding MeCz-Hz, consistent with a low trap density (Fig. 3E). PL and tr-PL evaluations of perovskite films deposited on bare FTO substrate consistently revealed enhanced PL intensity and extended carrier lifetimes, as well as bottom-excited measurements, further confirming

suppression of trap-assisted recombination in both bulk and at interfaces through improved defect management (figs. S64 to S66, tables S2 and S3). Further defect formation energy calculations confirmed the passivation effects of Hz-related species (figs. S67 and S68).

In addition to lowering recombination, the photoluminescence quantum yields (PLQY) enhancement observed for FTO/SAM/perovskite corresponded to an increased quasi-Fermi level splitting (QFLS), consistent with a stronger interfacial field effect arising from the intrinsic hole selectivity of the SAM. Introducing Hz further boosts PLQY and, accordingly, QFLS, which supports more efficient charge extraction (Fig. 3F). Additionally, transient photovoltage and photocurrent (TPV/TPC) measurements on the full device stack can decouple recombination and transport. The longer TPV response with Hz indicates suppressed recombination, while the faster TPC response is consistent with improved carrier collection and transport (figs. S69 and S70, and tables S4 and S5).

Device performance

We systematically evaluated the impact of Hz additives on device performance with a 5 × 4 orthogonal matrix that paired the four designed Hz additives with four SAM-based hole-selective layers (HSLs), encompassing all structural variations of our SAM and additive libraries. For each condition, 24 devices were fabricated to enable robust statistical comparisons (Fig. 4A, figs. S71 to S75, and tables S6 to S13). DBCz-Hz and MeCz-Hz, in particular, tended to increase open-circuit voltage (V_{OC}) across multiple SAM platforms, which stemmed from the stronger semiconducting character of their R groups. Across the full matrix, every Hz additive improved performance relative to additive-free controls, regardless of the underlying SAM. Notably, the largest performance gains were concentrated along the diagonal of the matrix, where each Hz additive was paired with its chemically matched SAM (i.e., Cz-Hz with 2PACz, MeO-Hz with MeO-2PACz, DBCz-Hz with 4PADCB, and MeCz-Hz with Me-4PACz).

In our experiments, among the SAMs tested, Me-4PACz delivered the best baseline performance, with an average PCE of 26.3% for control devices (0.06 cm^2). Introducing the matched MeCz-Hz additive increased the average PCE to 27.5% and reached a champion PCE of 27.7% (0.06 cm^2) (versus 26.4% for the control) (fig. S76). For the champion device, V_{OC}, short-circuit current density (J_{SC}), and fill factor (*FF*) increased from 1.19 V, 26.3 mA cm^{-2}, and 84.7% to 1.21 V, 26.6 mA cm^{-2}, and 85.9%, respectively (Fig. 4B). The J_{SC} obtained from *J*–*V* measurement agreed well with the value integrated from EQE (fig. S77). This champion device received an independent certification, confirming a fast-scan PCE of 27.6% with V_{OC} = 1.21 V, J_{SC} = 26.6 mA cm^{-2} and *FF* = 85.6%, along with a stabilized power output (SPO) efficiency of 27.4% (Fig. 4C and fig. S78).

Enabled by the widened processing window and the resulting gains in film uniformity, this strategy is well positioned for translation

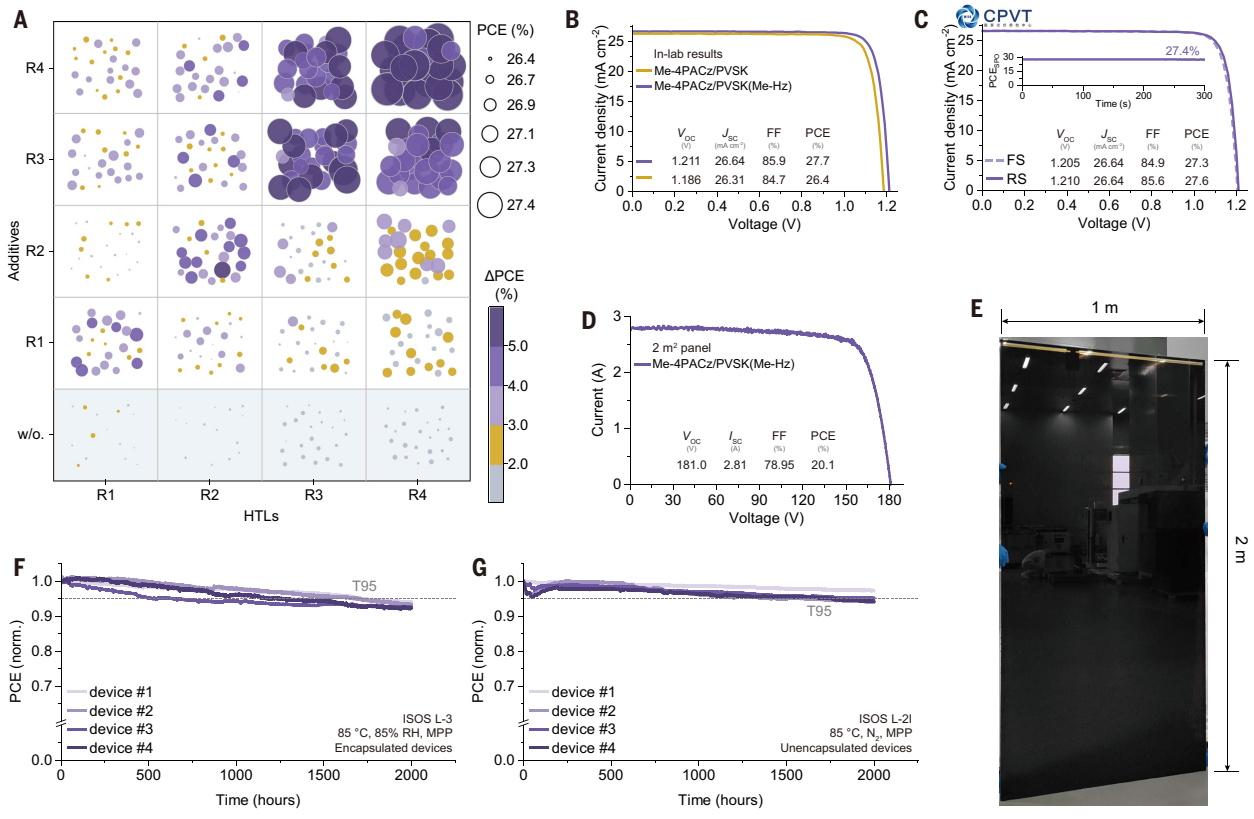

Fig. 4. Device performance. (**A**) Bubble plot summarizing statistical power conversion efficiency (PCE) results in a 5 × 4 orthogonal matrix that pairs Hz additives with hole-selective layers (HSLs). Bubble size represents the absolute PCE level. Bubble fill color represents the relative PCE gain, expressed as ΔPCE. For each HSL, the minimum PCE from the additive-free batch was used as the reference value (PCE_{ref}), and ΔPCE was calculated as $\Delta PCE = (PCE - PCE_{ref})/PCE_{ref}$. (**B**) Laboratory-scale *J*–*V* curves of the champion device on Me-4PACz with and without Hz additive, with photovoltaic parameters annotated. (**C**) Laboratory-scale *J*–*V* curve of the champion device certified by the National Center of Inspection on Solar Photovoltaic Products Quality (CPVT), with the certified stabilized power output (SPO) shown in the inset and photovoltaic parameters annotated. (**D**) *J*–*V* curves of champion large-area modules fabricated using the Hz additive strategy, with an active area of 2 m^2; the SPO is shown in the inset and photovoltaic parameters are annotated. (**E**) Photograph of a champion module with dimensions of 1 m × 2 m. (**F** and **G**) Thermal-stability aging of devices fabricated using the Hz additive strategy under (F) ISOS L-3 and (G) ISOS L-2L protocols. Four devices were measured for each protocol, and test conditions are provided in the plots. The initial PCE of four parallel samples for ISOS L-3 tests are 26.7%, 26.7%, 26.9%, and 27.0%. The initial PCE of four parallel samples for ISOS L-2I tests are 26.5%, 26.6%, 26.8%, and 26.8%.

beyond small-area devices. To demonstrate scalability and future applicability, we fabricated 1 m × 2 m perovskite panels with a specific active area of 2.0 m^2. The MeCz-Hz module achieved a champion PCE of 20.1%, corresponding to a power output of 402 W, with V_{OC} = 181 V, I_{SC} = 2.81 A and *FF* = 79.0% (Fig. 4, D and E). We also evaluated the effectiveness of the Hz additives with broader solvent systems, confirming their efficacy in improving device performance through beneficial modifications (fig. S79).

In the presence of the side redox cycle, the device stability could be degraded by the volatility of redox-generated I_2/I_3^- (*24*, *45*), the instability of iodine–DMSO adduct residues (**2**) (*30*), and the possibility of continued reactions driven by residual solvent in the film (*46*). We further examined operational stability with a focus on thermal durability. Stability was evaluated with two standard ISOS protocols with four parallel devices per condition, ISOS L-2I MPPT under 1 sun at 85°C in an inert atmosphere) and ISOS L-*3* (MPPT under 1 sun at 85°C and 85% RH). Hz-treated devices showed substantially improved durability, reaching a T95 lifetime of ~2000 hours under ISOS L-2I (Fig. 4G) and ~1500 hours under ISOS L-*3* (Fig. 4F).

Discussion

Our results uncover a previously overlooked wet-chemical limitation of carbazole-based phosphonic acid SAM contacts in p-i-n perovskite photovoltaics. We demonstrate that the dynamic SAM–perovskite interaction occurs not only under device operation stress but already initiates during film formation through the wet chemical redox process. During coating, the intrinsic phosphonic acidity of SAMs triggers and accelerates a DMSO-mediated redox cycle that generates detrimental I_2/I_3^- and iodine–DMSO adducts. These species accumulate on processing timescales and become imprinted into the forming film, distorting buried-interface lattice and electronic continuity, increasing deep traps, and thus degrading both initial PCE and operational stability of devices. Importantly, these effects are amplified under the longer wet windows required for large-area manufacturing.

Guided by this mechanism, we introduce conjugated hydrazide additives that sequester SAM-derived protons, suppress DMSO activation, and redirect solution speciation toward benign Hz–FA adducts. Beyond inhibiting redox chemistry, these adducts improve interfacial energetic continuity and promote vertical hole extraction, linking chemical control to electronic-function gains, consequently resulting in improved device performance. The broad performance improvements across multiple SAM/additive pairs indicate that "chemical compatibility" is a design axis orthogonal to semiconducting properties. More generally, managing acid-driven redox in polar solvents should be transferable to other optimizations within PSCs and scalable coating routes where interfacial dissolution and extended wet times are unavoidable.

REFERENCES AND NOTES

1. Z. Xiong *et al.*, *Science* **390**, 638–642 (2025).
2. Z. Li *et al.*, *Science* **382**, 284–289 (2023).
3. W. Peng *et al.*, *Science* **379**, 683–690 (2023).
4. S. Zhang *et al.*, *Science* **380**, 404–409 (2023).
5. S. Liu *et al.*, *Nature* **632**, 536–542 (2024).
6. S. M. Park *et al.*, *Nature* **624**, 289–294 (2023).
7. K. Zhao *et al.*, *Nature* **632**, 301–306 (2024).
8. W. Jiang *et al.*, *Nature* **646**, 95–101 (2025).
9. C. Liu *et al.*, *Science* **382**, 810–815 (2023).
10. H. Chen *et al.*, *Science* **384**, 189–193 (2024).
11. Q. Tan *et al.*, *Nature* **620**, 545–551 (2023).
12. X. Zheng *et al.*, *Nat. Energy* **8**, 462–472 (2023).
13. A. Al-Ashouri *et al.*, *Science* **370**, 1300–1309 (2020).
14. M. Li, M. Liu, F. Qi, F. R. Lin, A. K.-Y. Jen, *Chem. Rev.* **124**, 2138–2204 (2024).
15. M. A. Truong *et al.*, *J. Am. Chem. Soc.* **147**, 2797–2808 (2025).
16. H. Tang *et al.*, *Science* **383**, 1236–1240 (2024).
17. B. Dong *et al.*, *Nat. Energy* **10**, 342–353 (2025).
18. C. Fei *et al.*, *Science* **391**, eadz7969 (2026).
19. W. S. Yang *et al.*, *Science* **348**, 1234–1237 (2015).
20. J. Wang *et al.*, *Nat. Commun.* **16**, 4148 (2025).
21. Y. Liang *et al.*, *Nature* **648**, 91–96 (2025).
22. H. Wei *et al.*, *Adv. Funct. Mater.* **36**, e16987 (2025).
23. Y. Ma *et al.*, *Angew. Chem. Int. Ed.* **64**, e202504253 (2025).
24. M. A. Uddin *et al.*, *Nat. Commun.* **15**, 1355 (2024).
25. Y. Ashikari, A. Shimizu, T. Nokami, J. Yoshida, *J. Am. Chem. Soc.* **135**, 16070–16073 (2013).
26. T. A. S. Doherty *et al.*, *Science* **374**, 1598–1605 (2021).
27. D. J. Kubicki, S. D. Stranks, C. P. Grey, L. Emsley, *Nat. Rev. Chem.* **5**, 624–645 (2021).
28. E. A. Alharbi *et al.*, *Nat. Commun.* **10**, 3008 (2019).
29. L. Tian *et al.*, *J. Energy Chem.* **109**, 368–377 (2025).
30. S. Song *et al.*, *Nat. Catal.* **3**, 107–115 (2019).
31. Z. W. Qu, H. Zhu, S. Grimme, *ChemCatChem* **13**, 207–211 (2020).
32. P. Kumar Verma, R. A. Vishwakarma, S. D. Sawant, *Asian J. Org. Chem.* **8**, 777–801 (2019).
33. H. Liao, Z. Huang, Q. Zhu, *Org. Biomol. Chem.* **20**, 3721–3725 (2022).
34. Q. Jiang *et al.*, *Nature* **611**, 278–283 (2022).
35. A. A. Ordinartsev *et al.*, *Acta Crystallogr. E Crystallogr. Commun.* **77**, 692–695 (2021).
36. D. Fishman, "Ramen correlations" [accessed July 2026]; https://www2.chemistry.msu.edu/faculty/reusch/virttxtjml/spectrpy/infrared/infrared.htm.
37. Y. Zhang *et al.*, *Science* **387**, 284–290 (2025).
38. M. Qin *et al.*, *Adv. Mater.* **31**, e1901284 (2019).
39. P. Zhu *et al.*, *Science* **383**, 524–531 (2024).
40. A. Telfah *et al.*, *Polym. Bull.* **79**, 3759–3778 (2021).
41. Z. Liang *et al.*, *Nature* **624**, 557–563 (2023).
42. W. Reusch, "Infrared spectroscopy" (2013); https://www2.chemistry.msu.edu/faculty/reusch/virttxtjml/spectrpy/infrared/infrared.htm.
43. R. Azmi *et al.*, *Nature* **628**, 93–98 (2024).
44. T. Li *et al.*, *Nat. Energy* **8**, 610–620 (2023).
45. S. Chen, X. Xiao, H. Gu, J. Huang, *Sci. Adv.* **7**, eabe8130 (2021).
46. M. Wang, C. Fei, M. A. Uddin, J. Huang, *Sci. Adv.* **8**, eabo5977 (2022).
47. Z. Liang *et al.*, *Nat. Mater.* **25**, 267–274 (2026).
48. Z. Liang *et al.*, Redirecting wet-interfacial redox pathways for efficient inverted perovskite solar cells (Demo Dataverse, 2026); doi: 10.70122/FK2/XVN39T.

ACKNOWLEDGMENTS

The authors acknowledge support from Wilson Tang Brilliant Energy Science and Technology Lab (BEST Lab) and Materials Characterization & Preparation Facility (MCPF) at HKUST (Guangzhou) for their facilities and technical support. This work was supported by the Hong Kong University of Science and Technology (Guangzhou) startup grant (G0101000267) and the Guangzhou-HKUST(GZ) Joint Funding Program (2023A03J0003). Y.Z. acknowledges the Youth S&T Talent Support Programme of Guangdong Provincial Association for Science and Technology (GDSTA) (SKXRC2025469). N.-G.P. acknowledges financial support through grants from the National Research Foundation of Korea, which is funded by the Korean government (MSIT and MOE) under contracts NRF-2021R1A3B1076723 (Research Leader Program) and RS-2026-25501632 (NRL 2.0). Y.L.L. acknowledges the long-term financial support from CATL. We thank the Harvard Dataverse for providing a reliable platform for sharing and archiving research data (*48*). **Author contributions:** Z.L. conceived the central idea and designed the additives. Y.Z. supervised this project and oversaw project administration. Z.L. and B.L. fabricated the laboratory-scale devices and carried out most measurements. Y.L.L., G.C., B.T., C.Z., and C.O. fabricated the meter-scale panel. Y.L.Z. performed and analyzed optoelectronic characterizations. Y.Y. and C.L. contributed to conceptual interpretation and mechanism discussion. S.C. and Y.B. conducted structural and surface analyses. H.L. and H.X. supported chemical analyses. M.F. performed Raman measurements. P.Z. and X.Y.Z. carried out electrical tests. H.Z. advised on molecular synthesis route design. X.F.Z. and C.Q.L. performed GIWAXS measurements. Y.H.L. contributed to computational studies. Y.Z. and N.-G.P. secured funding. Z.L. and B.L. wrote the original draft. Z.L., Y.Z., Y.L.L., Y.L.Z., Y.Y., C.L., L.M., C.Z., and N.-G.P. revised the manuscript. All authors discussed the results and commented on the manuscript. **Competing interests:** Z.L. and Y.Z. are inventors on patent application (CN202611023616.X) related to the core concept of this manuscript, including the synthesis of additive materials and their application in perovskite photovoltaics, submitted by the Hong Kong University of Science and Technology (Guangzhou). The other authors declare that they have no competing interests. **Data, code, and materials availability:** All data and details of materials synthesis are available in the main text or the supplementary materials.

SUPPLEMENTARY MATERIALS

science.org/doi/10.1126/science.aeg8415
Materials and Methods; Figs. S1 to S79; Tables S1 to S14; References (*49*–*59*)

Submitted 1 March 2026; accepted 1 July 2026

10.1126/science.aeg8415

Redirecting wet–interfacial redox pathways for efficient inverted perovskite solar cells

Zheng Liang, Boyuan Liu, Yuelong Li, Yalan Zhang, Yi Yang, Shengbin Cheng, Linchuan Ma, Bao Tu, Hua-Chao Liu, Huifen Xu, Yuqi Bao, Minghui Fan, Peide Zhu, Xianfu Zhang, Congqi Li, Hui Zhang, Xinyuan Zhang, Yuheng Li, Guodong Chen, Cheng Liu, Chen Zhu, Chuying Ouyang, Nam-Gyu Park, and Yong Zhang

Science **393** (6813), . DOI: 10.1126/science.aeg8415

Editor's summary

Conjugated hydrazide additives limit the adverse effect of protons from hole-selective contacts with perovskite inks. Liang *et al*. found that the acidity of carbazole-based phosphonic self-assembled monolayers triggered detrimental iodide redox reactions mediated by the dimethyl sulfoxide used in perovskite precursors. Hydrazine additives suppressed this reaction and created benign adducts with formamidinium cations. Certified power conversion efficiencies of 27.4% were achieved in small-area cells, and unencapsulated devices retained 95% of their efficiency after about 1500 hours of maximum power point tracking at 85°C and 85% relative humidity. —Phil Szuromi